Appl. Math. Mech. -Engl. Ed., **42**(8), 1095–1108 (2021)

APPLIED MATHEMATICS AND MECHANICS (ENGLISH EDITION)

https://doi.org/10.1007/s10483-021-2761-9

Typical transient effects in a piezoelectric semiconductor nanofiber under a suddenly applied axial time-dependent force*

Wanli YANG†, Yuxing LIANG

Department of Mechanics, School of Aerospace Engineering, Hubei Key Laboratory of Engineering Structural Analysis and Safety Assessment, Huazhong University of Science and Technology, Wuhan 430074, China

(Received Apr. 25, 2021 / Revised Jun. 11, 2021)

Abstract Based on the mechanical motion equation, Gauss's law, and the current continuity condition, we study a few typical transient effects in a piezoelectric semiconductor (PS) fiber to realize the startup and turning-off functions of common piezotronic devices. In this study, the transient extensional vibration induced by a suddenly applied axial time-dependent force is examined in a cantilevered n-type ZnO nanofiber. Neither the magnitude of the loadings nor the doping concentration significantly affects the propagation caused by disturbance of the axial displacement. However, both of the factors play an important role in the propagation caused by disturbance of the electron concentrations. This indicates that the electromechanical coupling effect can be expected to directly determine the electronic performance of the devices. In addition, the assumption of previous simplified models which neglect the charge carriers in Gauss's law is discussed, showing that this assumption has a little influence on the startup state when the doping concentration is smaller than $10^{21}\,\mathrm{m}^{-3}$. This suggests that the screening effect of the carriers on the polarized electric field is much reduced in this situation, and that the state is gradually transforming into a pure piezoelectric state. Nevertheless, the carriers can provide a damping effect, which means that the previous simplified models do not sufficiently describe the turning-off state. The numerical results show that the present study has referential value with respect to the design of newly multifunctional PS devices.

Key words transient, piezoelectric semiconductor (PS), extension, vibration

Chinese Library Classification O472$^+$.91
2010 Mathematics Subject Classification 82D37

1 Introduction

Piezoelectric semiconductors (PSs) have recently attracted widespread interest for the design of multifunctional devices owing to their additional piezoelectric properties[1] compared with

* Citation: YANG, W. L. and LIANG, Y. X. Typical transient effects in a piezoelectric semiconductor nanofiber under a suddenly applied axial time-dependent force. *Applied Mathematics and Mechanics* (*English Edition*), **42**(8), 1095–1108 (2021) https://doi.org/10.1007/s10483-021-2761-9

† Corresponding author, E-mail: wanli_yang_nt1@163.com

Project supported by the National Natural Science Foundation of China (No. 11972164) and the Key Laboratory Project of Hubei Province of China (No. 2016CFA073)

general Si semiconductors. In these materials, the mechanical stimuli and electrical properties can interact directly because these materials have both piezoelectric and semiconducting properties. This gives rise to the appearance of a novel device application known as "piezotronics", including nanogenerators[2–4], acoustic charge transport devices[5], field effect transistors[6–9], as well as chemical sensors[10]. Recently, the static behavior of ZnO PS structures with high performance was reported[11–15]. However, in spite of significant developments in these applications, the field of piezotronics still presents various challenges as a result of coupling among the multiple physical properties and mathematical problems, especially in time-dependent applications[16].

It is well known that the time-dependent behaviors of PS structures are more important to the devices than the above-mentioned static ones, for example, in applications such as frequency generation/operation, telecommunication, time keeping, and sensing[17]. However, most of the existing analyses of PS structures only considered the I-V characteristics in the steady-state[18–21], wave propagation[22–26], or time-harmonic vibration[27]. Although the above analyses can extract the most basic behaviors of PS structures including their resonant frequencies and mode shapes, important transient effects in device operations still cannot be described. For example, for acoustic charge transport devices, startup and turning off are unavoidable transient processes. Moreover, fluctuations in the driving force or voltage are known to induce transient effects in a harmonic operation[17]. It is noted that such important applications have been widely investigated in quartz resonators[28], which motivated the present study with the aim of extending it to important PS devices. Apart from this, the transient behaviors of PS devices are strongly related to the factors including the properties and geometric configurations of a material. The transient vibration analysis with a time-independent stimulus was recently reported. These studies showed that the use of external triggers as stimulus also determines the transient behaviors of PS devices in addition to the above-mentioned intrinsic factors[29–30]. However, the carriers in Gauss's equation were neglected in Refs. [29] and [30] followed by Refs. [12] and [31] to decouple the multi-field coupling equations that would have enabled analytical results to be obtained. It is noted that this assumption resulted in the system being opened, although it is convenient for the purpose of calculation. Furthermore, the time-dependent stimulus is more general than those static ones in engineering applications.

Therefore, the transient process of a cantilevered n-type ZnO nanofiber is analyzed in this study under time-dependent forces that are suddenly applied along the c-axis. Multi-field coupling equations are numerically solved for the fully coupled state and compared with those that are approximately decoupled to validate the application scope of the previous simplified models. Then, the typical transient effects are further analyzed for different loadings and doping concentrations. Finally, conclusions are drawn that are of significance for both the design and practical application of PS devices.

2 One-dimensional (1D) equations for the extension of a PS fiber

In this section, 1D equations for the extension of a PS fiber are presented. It is well known that a 1D model has sufficient accuracy to model rod-like structures with a high span ratio. As shown in Fig. 1, a cantilevered n-type ZnO fiber is considered with an arbitrary cross section

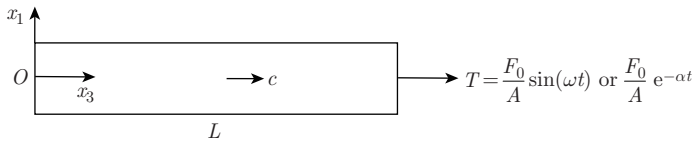

Fig. 1 PS fiber of crystals of class 6 mm

A, and its length L is much larger than the characteristic dimension of the cross section. At $t = 0\,\mathrm{s}$, the free end is subject to a suddenly applied extensional force F or stress $T = F/A$. In Fig. 1, the c-axis of the crystal coincides with the long axis of the fiber. The extensional forces are taken as sinusoidal and exponential forms, in which ω, F_0, and α are the angular frequency, the initial magnitude of the force, and the attenuation coefficient, respectively. In addition, the surface of the fiber is unelectroded. The electric field in the surrounding free space is neglected, an approximation that is commonly made.

For a 1D n-type ZnO fiber, the mechanical motion equation, Gauss's law, and the current continuity condition can be expressed as

$$T_{3,3} = \rho \ddot{u}_3, \tag{1a}$$

$$D_{3,3} = -q\Delta n, \tag{1b}$$

$$J^n_{3,3} = q\Delta \dot{n}. \tag{1c}$$

In the above equation, T_3, u_3, D_3, and J^n_3 are the axial stress, the displacement, the electric displacement, and the current density of electrons, respectively. ρ is the mass density, q is the electronic charge, Δn denotes the disturbance of electrons, and "$(\cdot)_{,3}$" denotes the derivative with respect to the coordinate x_3. In addition, a superimposed dot represents a time derivative.

The relevant 1D constitutive relations are

$$T_3 = \overline{c}_{33} S_3 - \overline{e}_{33} E_3, \tag{2a}$$

$$D_3 = \overline{e}_{33} S_3 + \overline{\varepsilon}_{33} E_3, \tag{2b}$$

$$J^n_3 = q N_{\mathrm{D}} \mu^n_{33} E_3 + q D^n_{33} \Delta n_{,3}, \tag{2c}$$

in which the drift current of electrons is linearized, as in Refs. [11], [14], [21], and [22], with a small Δn. Here, N_{D} denotes the initial doping concentration, and μ^n_{33} and D^n_{33} are the carrier mobility and diffusion constants of the electrons, respectively. The stress relaxation is used by considering Poisson's effect. Therefore, the parameters in Eq. (2) are modified. $\overline{c}_{33}$, $\overline{e}_{33}$, and $\overline{\varepsilon}_{33}$ are the effective elastic, piezoelectric, and dielectric constants, respectively, which can be obtained from Ref. [11].

Without loss of generality, the axial strain S_3 and the electric field E_3 are the gradients of the mechanical displacement and the electric potential, which can be defined as

$$S_3 = u_{3,3}, \quad E_3 = -\varphi_{,3}. \tag{3}$$

The conditions for determining the solutions are given as follows:

$$\begin{cases} u_3 = 0, \quad D_3 = 0, \quad J_3 = 0 \quad \text{at} \quad x_3 = 0, \\ T_3 = T, \quad D_3 = 0, \quad J_3 = 0 \quad \text{at} \quad x_3 = L, \\ u_3 = 0, \quad \dot{u}_3 = 0, \quad \varphi = 0, \quad \Delta n = 0 \quad \text{at} \quad t = 0. \end{cases} \tag{4}$$

It is noted that the multi-coupled equation (1) can be numerically solved by using the finite element method (FEM) with the boundary and initial conditions in Eq. (4). Because there are no boundary conditions prescribed directly on the electric potential, the electric potential may have an arbitrary constant which does not make any difference to the electric field it produces. For uniqueness, we let $\varphi = 0$ at $x_3 = 0$. However, it is noted that the approximate analytical solutions can be obtained by neglecting part of weak interactions as reported in Refs. [29]–[31]. The advantage of these analytical solutions is that they are helpful to reveal the essence of some physical phenomena, although the scope of applications of the introduced assumptions needs to be further verified. Therefore, the approximately theoretical analysis is also presented in Appendix A as a comparison.

3 Numerical results and discussion

As usual, the cross section of the fiber is a circle, and the area of the section is taken as $A = 2.598 \times 10^{-14}\,\mathrm{m}^2$[11]. As an example, the material constants of the ZnO fiber were obtained from Ref. [32]. $L = 600\,\mathrm{nm}$, $N_\mathrm{D} = 10^{20}\,\mathrm{m}^{-3}$, and $F_0 = 1.7\,\mathrm{nN}$ unless otherwise stated. The development of 5G has resulted in the widespread use of medium-high frequency devices in mobile communications, such as antennas, filters, radio frequency switches, and power amplifiers. It is noted that their working frequencies usually range from several to tens of GHz. In addition, the resonance frequencies of the ZnO fiber are in the range of GHz[27]. Therefore, we take $f = \omega/(2\pi) = 30\,\mathrm{GHz}$ in this paper to move away from the first resonance frequency. Moreover, the attenuation coefficient α is the same as ω in terms of its value.

First, we examine the accuracy of u_3 and Δn obtained by using the FEM. At one arbitrary moment, we take $t = 10.8 \times 10^{-11}\,\mathrm{s}$ as an example (a special time point will be discussed in the next). We use the FEM to solve the fully coupled equation (1) without approximation, and compare it with the results obtained from the approximate analytical solutions in Appendix A by $m = 20$ and $r = 7$. As shown in Fig. 2, both the solutions are completely coincident, which indicates that the approximation taken in the series solutions has a little influence on the transient performance in this case. In addition, it is verified at the other time instants that they are all in good correspondence. This is because $N_\mathrm{D} = 10^{20}\,\mathrm{m}^{-3}$ is a low doping concentration, such that the coupling effect between the carriers and mechanical-electric fields is weak. Therefore, the simplified analytical model is valid. However, the critical doping concentration for a valid approximation will be further examined.

The distributions of u_3 along the fiber disturbed by the suddenly sinusoidal and exponential

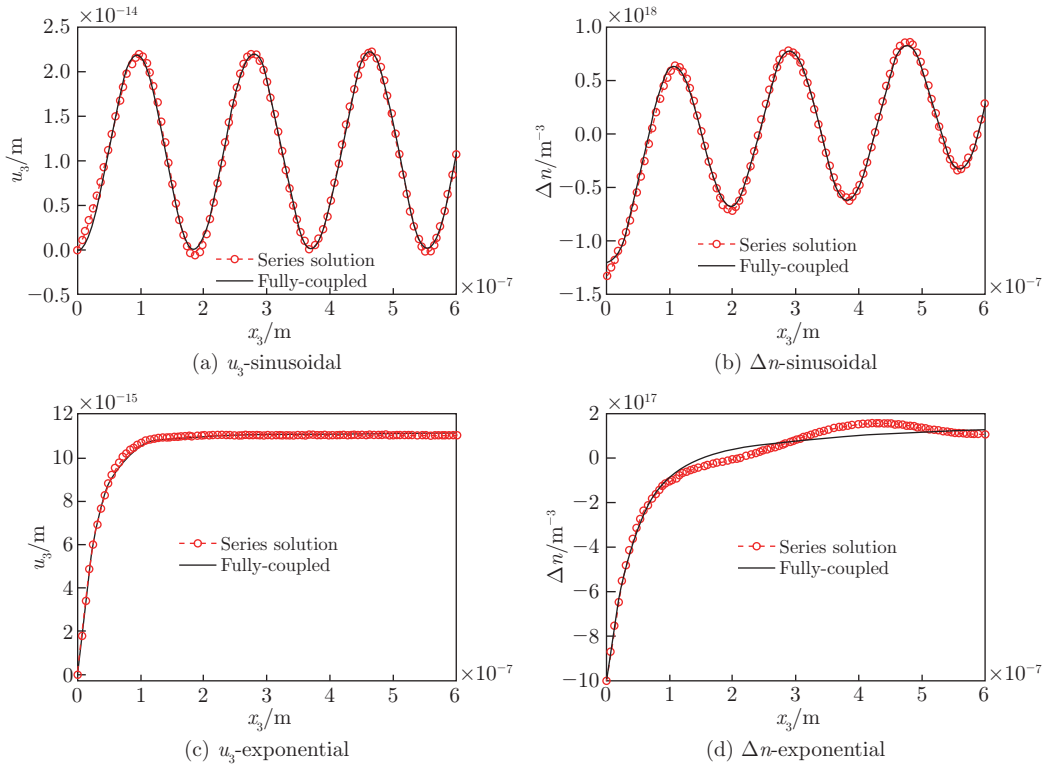

Fig. 2 Comparisons of FEM results with series solutions at $t = 10.8 \times 10^{-11}\,\mathrm{s}$ (color online)

axial ending forces are analyzed at different time instants in Fig. 3, in which Figs. 3(a) and 3(b) show the initial disturbance for suddenly applied sinusoidal ending forces and Figs. 3(c) and 3(d) show the initial disturbance for an exponential ending force. Compared with Fig. 2, it is observed that the response time of the disturbance in the fiber is approximately 10.8×10^{-11} s in both loading cases, i.e., the time at which the disturbance propagates through the entire fiber. This process can be used to describe the startup state of the PS devices at $t = 0$ s from rest, for instance, acoustic charge transport devices. Interestingly, the response time 10.8×10^{-11} s is close to $L/\sqrt{c_{33}^*/\rho}$, which corresponds to the wave speed by considering the piezo-effect with an additional electric stiffness. This is caused by the low doping concentration and high vibration frequency, such that the disturbance propagates near the pure piezoelectric wave speed. In addition, it has been proved in Ref. [33] that only weak dispersion happened in the intermediate frequency range for this mechanical disturbance, which showed that the propagation speed ranges from that in the pure elastic state, that is, $\sqrt{\overline{c}_{33}/\rho}$, to that in the pure piezoelectric state. Because $\sqrt{c_{33}^*/\overline{c}_{33}} \approx 1.1$, the propagation speed of this mechanical disturbance is weakly dependent on the loading modes (see Fig. 3), the magnitude of the end force (see Figs. 5(a) and 5(b)), and the doping concentration (see Fig. 9).

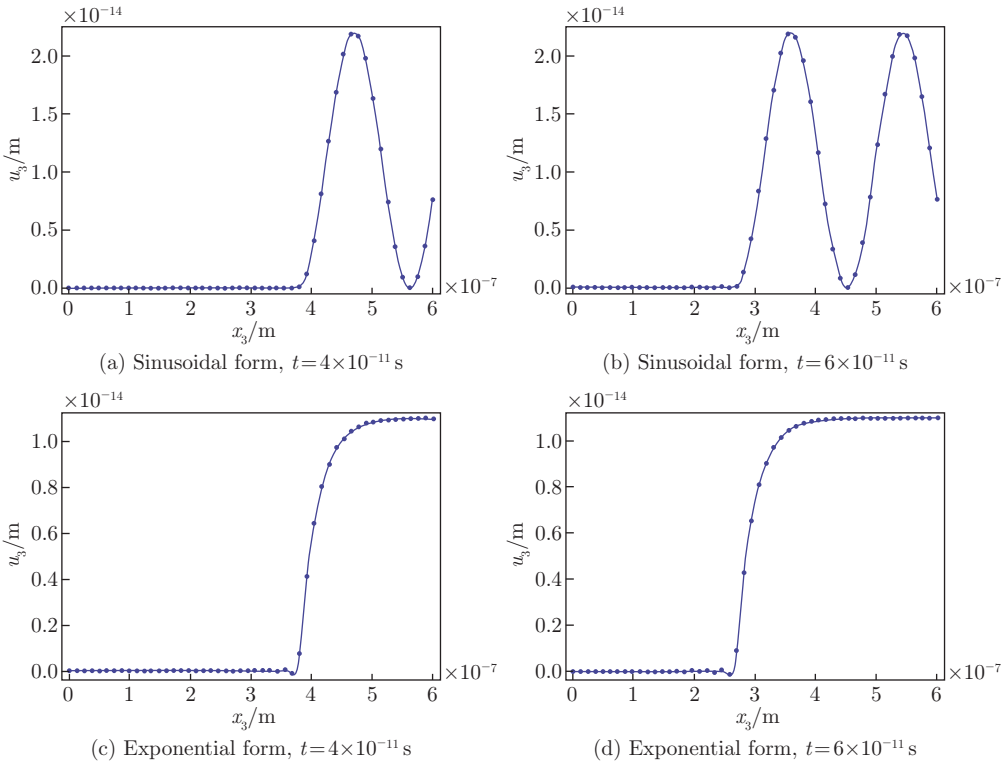

(a) Sinusoidal form, $t=4\times10^{-11}$ s

(b) Sinusoidal form, $t=6\times10^{-11}$ s

(c) Exponential form, $t=4\times10^{-11}$ s

(d) Exponential form, $t=6\times10^{-11}$ s

Fig. 3 Distributions of u_3 along the fiber at different time instants and for various loading modes (color online)

Corresponding to the time instants in Fig. 3, the distributions of Δn along the fiber are shown in Fig. 4. The response time of Δn in the fiber, which differs fundamentally from the distribution of the displacement u_3 along the fiber, is much less than that of u_3. Thus, in this case, the devices are able to detect the electrical signals faster than the mechanical signals. This can be attributed to the newly associated wave induced by the interaction between the movable carriers and polarized electric field[33]. The propagation speed of this associated wave is much

larger than the generalized mechanical wave at high frequencies[33]. The reason is that the disturbing electric field on the mechanical wave front will drive movement of the carrier, which results in the disturbance of Δn leading to u_3. Moreover, the loading mode has weak effects on the disturbance propagation speed of Δn, which is different from the displacement. The reason is that this associated wave is a strongly dispersive wave owing to the interaction between the movable electrons and the polarized electric field. Therefore, the propagation property may be highly dependent on the loading, which is obvious from Figs. 5(c) and 5(d). A similar phenomenon is shown in Fig. 10 for different doping concentrations. It can be numerically calculated that the integral of Δn over $[0, L]$ vanishes because the fiber is electrically isolated, which also validates the correctness of the present solutions. Moreover, it is observed that the variations of the displacements and electrons in the sinusoidal case are more obvious than those in the exponential case as expected, which indicates that the startup state is smoother in the latter case. In summary, the present results have referential value for the design of new multifunctional acoustic charge transport devices.

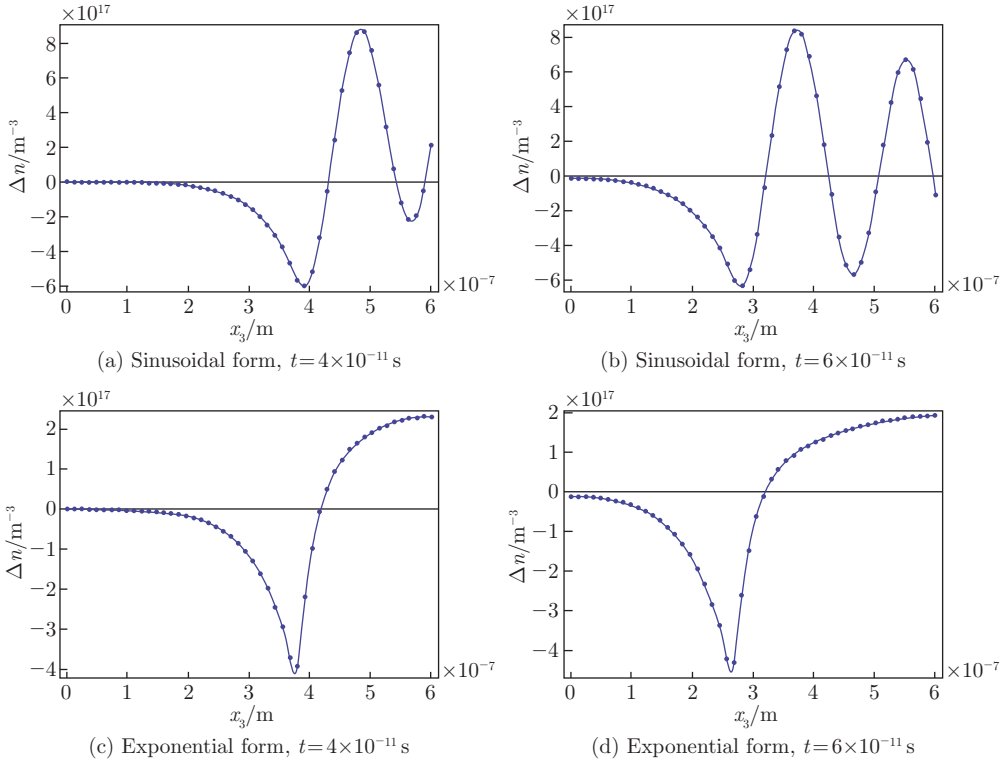

(a) Sinusoidal form, $t=4\times10^{-11}$ s (b) Sinusoidal form, $t=6\times10^{-11}$ s

(c) Exponential form, $t=4\times10^{-11}$ s (d) Exponential form, $t=6\times10^{-11}$ s

Fig. 4 Distributions of Δn along the fiber at different time instants and for various loading modes (color online)

In Fig. 5, we plot the distributions of u_3 and Δn along the fiber at a fixed $t = 6 \times 10^{-11}$ s with different magnitudes of applied F_0. Figure 5 shows that all u_3 and Δn become stronger, as expected. This means that the transient behaviors can be effectively tuned by the external forces, such that it can be used as a reference for designing and controlling the performance of electronic devices. It is also observed that the propagation speed of u_3 is independent of the magnitude of the end force because of the weak dispersion, as discussed above. However, the propagation speed of Δn is obviously highly dependent on F_0. This is because the disturbance of the electrons is driven by the polarized electric field. The increase in F_0 enhances the

polarized electric field, which further interacts with the motion of the electrons. Therefore, the electric-field/carrier interaction wave in Ref. [33] exhibited strong dispersion.

Figure 6 plots the operating state with the sinusoidal end force removed at $t = 3.3 \times 10^{-11}$ s. As expected, only one crest propagates in the fiber because the force is removed exactly at the first period. Therefore, the operating modes of these devices can be tuned by adjusting the action time of the force in the initial steady state. In addition, the moving carriers may

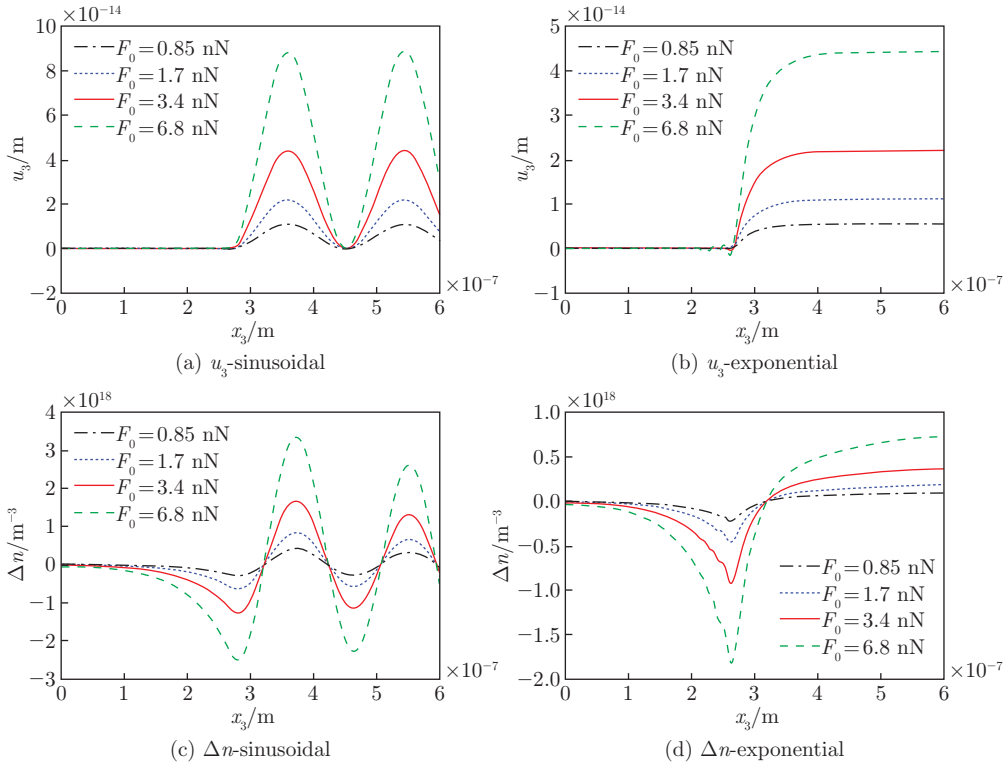

Fig. 5 Distributions of u_3 and Δn along the fiber at different applied F_0 at a fixed $t = 6 \times 10^{-11}$ s (color online)

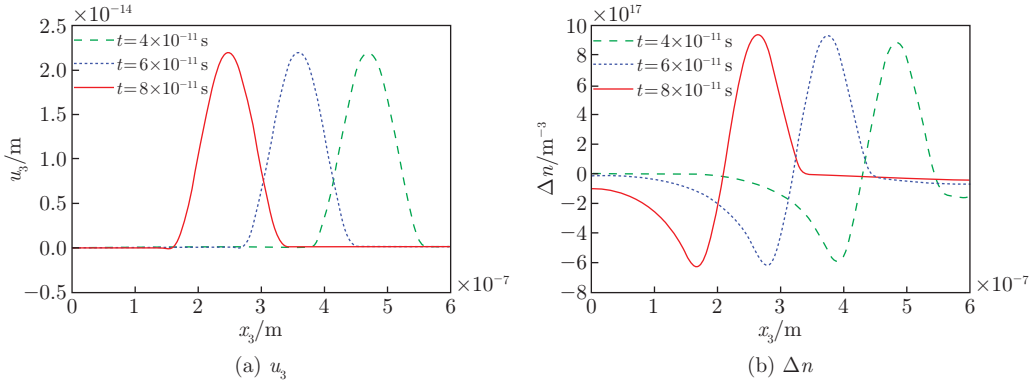

Fig. 6 Disturbance along the fiber at different time instants when the force is removed at $t = 3.3 \times 10^{-11}$ s (color online)

induce the damping effect, which indicates that the turning-off property can be described in this state. However, this process is often time consuming[28] such that the disturbance proceeds through many cycles. Thus, the turning-off properties are further analyzed and the results are shown in Figs. 7 and 8 for different doping concentrations. It should be noted that a doping concentration less than $10^{20}\,\mathrm{m}^{-3}$ is very low, which in turn causes a weak damping effect and extends the turning-off time. This is because the lower doping concentration transforms the PS fiber into a purely piezoelectric fiber. The wave propagation is known to undergo no dissipation in a purely piezoelectric fiber. Therefore, the doping concentration range from $10^{21}\,\mathrm{m}^{-3}$ to $10^{23}\,\mathrm{m}^{-3}$ is chosen to analyze the turning-off property. The results show that the present model can effectively capture the shutdown property and that the turning-off time is related to the doping concentration. In addition, it is interesting that a higher doping concentration does not necessarily correspond to stronger dissipation. The reason is that the propagation speed of the carriers is much reduced with the increasing doping concentration (see Fig. 10) such that less energy is directed away from the mechanical wave front by the new associated wave. Therefore, the damping effect is weakening. Furthermore, it should be noted that although the approximate solutions can accurately describe the startup properties in low doping cases (shown in Fig. 2), they are invalid for the turning-off properties because of the absence of dissipation in Eq. (A1b).

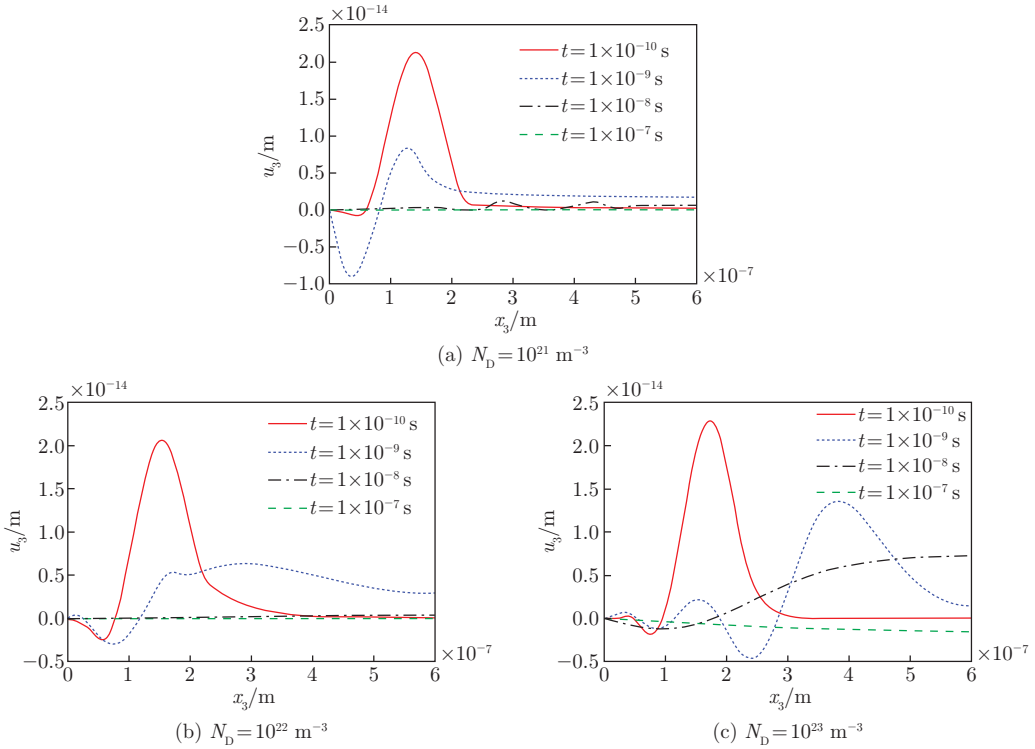

Fig. 7 Turning-off properties of u_3 at different doping concentrations (color online)

Finally, we consider the above important issue of validating the scope of an application regarding the approximation in different doping concentrations. Figures 9 and 10 show the effects of the approximation on the distribution of u_3 and Δn along the fiber at a fixed $t = 6\times10^{-11}$ s. The approximation adopted in Appendix A is observed to have a significant effect on the carrier distribution whereas it has a little influence on the displacement, which is quite different from the lower initial doping case, i.e., $N_D = 10^{20}\,\mathrm{m}^{-3}$ shown in Fig. 2. This means

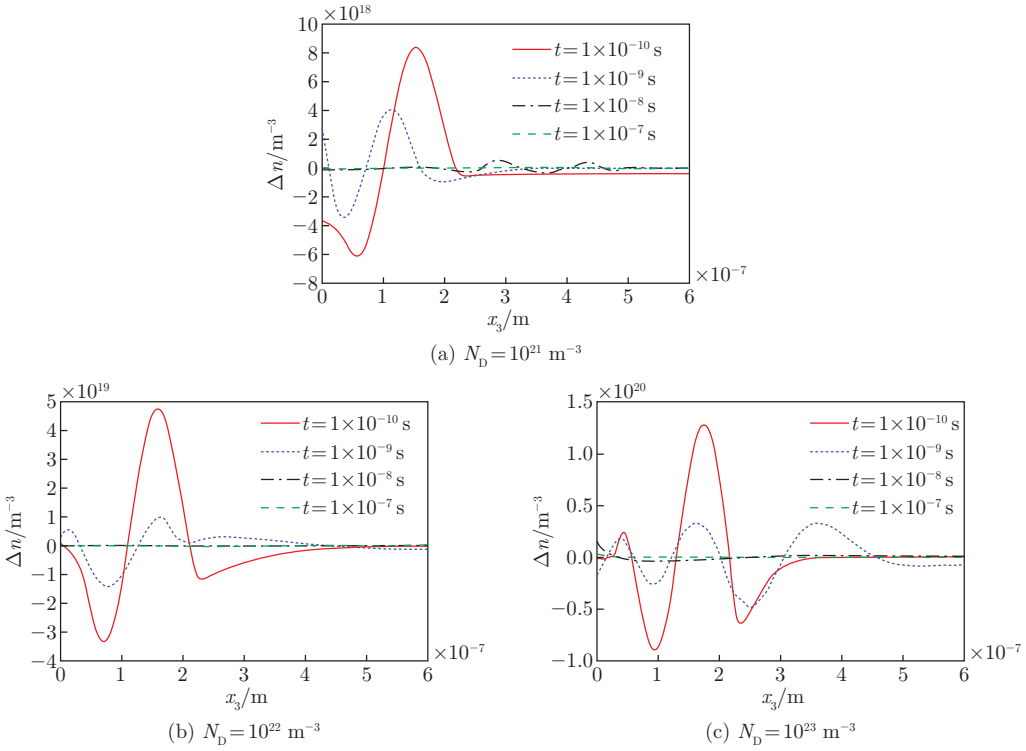

Fig. 8 Turning-off properties of Δn at different doping concentrations (color online)

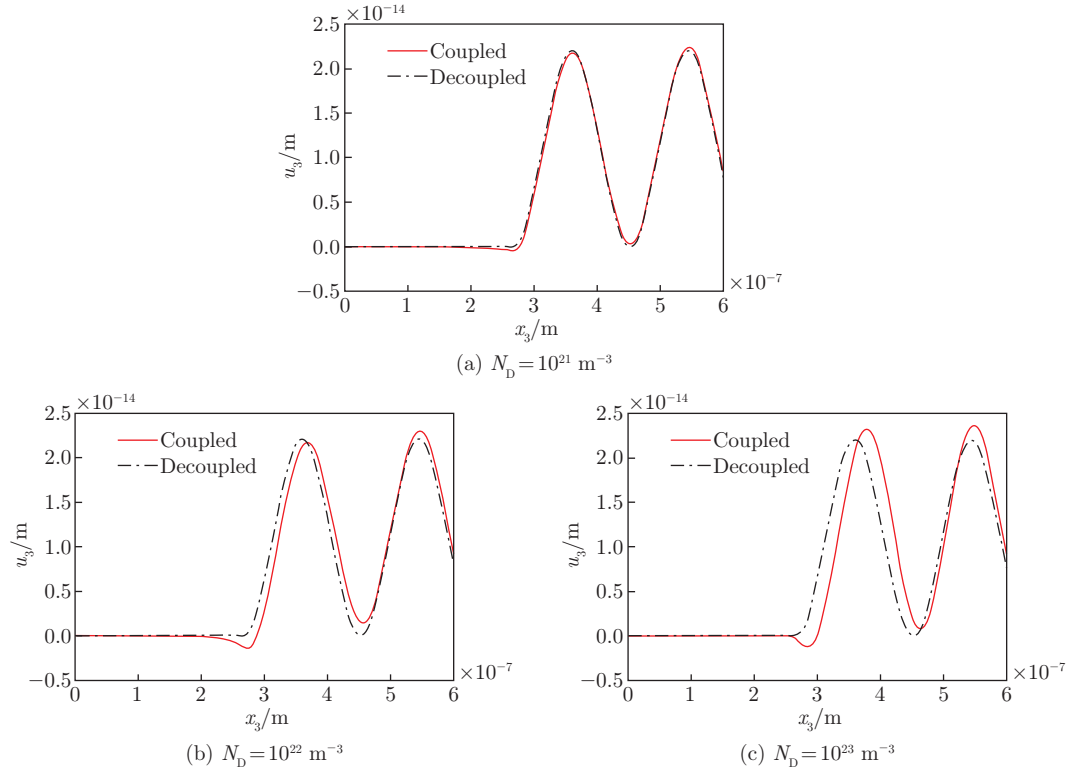

Fig. 9 Effects of the approximation on u_3 at a fixed $t = 6 \times 10^{-11}$ s (color online)

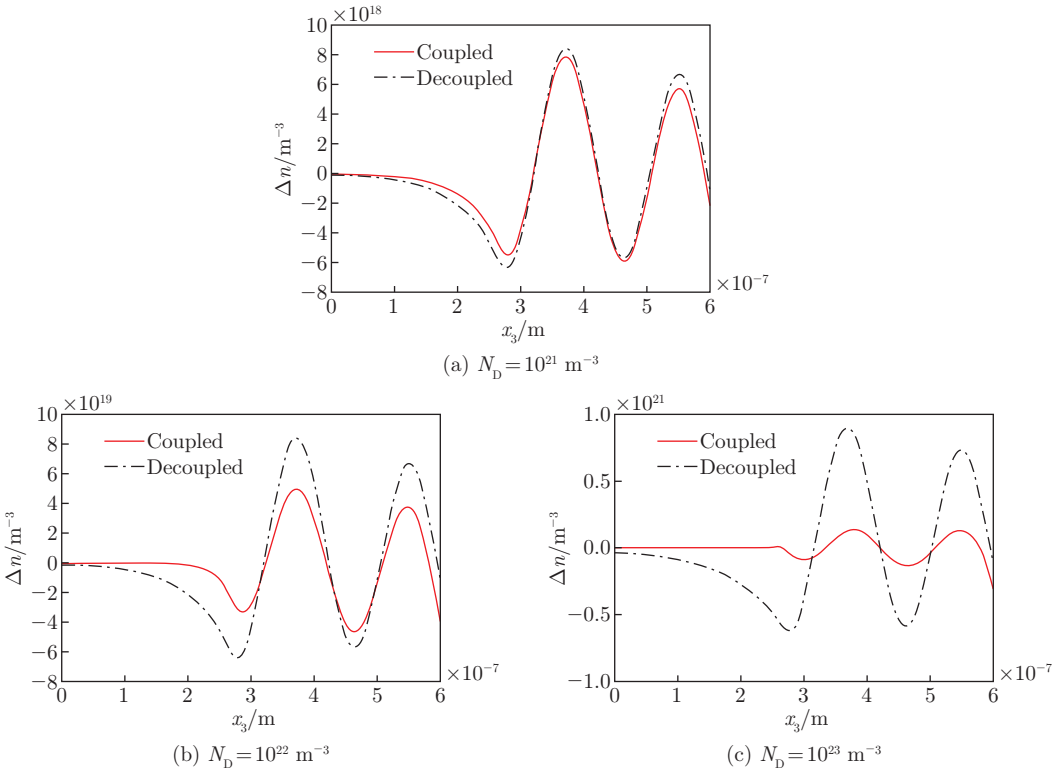

Fig. 10 Effects of the approximation on Δn at a fixed $t = 6 \times 10^{-11}$ s (color online)

that the doping concentration is a key factor responsible for determining the validation of the above approximation that was used in the theoretical analysis. Therefore, this approximation, which is made in many studies, can only be used for the initial lower doping concentrations. Moreover, it is noted that $N_{\mathrm{D}} = 10^{21}\,\mathrm{m}^{-3}$ is a critical doping concentration in this study. Once the doping concentration is over $N_{\mathrm{D}} = 10^{21}\,\mathrm{m}^{-3}$, the coupling effect of the carriers on the mechanical-electrical field is no longer negligible. Apart from this, it is observed that the response time of the electrons is enlarged considerably by increasing the doping concentration. This can be attributed to the screening effect of the carriers, such that the polarized electric field can be counteracted. In summary, the response or the turning-off time of the electrons can be tuned by adjusting the doping concentration.

4 Conclusions

Selected typical transient effects are accurately analyzed by applying time-dependent ending forces to a ZnO fiber. The startup and turning-off properties can be well described by the evolution of the displacement and carrier fluctuations. The results also show that the electrical signals can be detected faster than the mechanical signals at lower doping concentrations, which is useful in nondestructive testing. In addition, the transient performance can be effectively tuned by adjusting the action time, the magnitude of the applied force, and the doping concentration. Finally, the results presented here can be referenced to design nanosensors.

Acknowledgment We would like to sincerely thank Professor Jiashi YANG at the University of Nebraska and Professor Yuantai HU at Huazhong University of Science and Technology for their

helpful discussion and suggestions.

References

[1] WANG, Z. L. and WU, W. Z. Piezotronics and piezo-phototronics-fundamentals and applications. *National Science Review*, **1**, 62–90 (2013)

[2] GAO, P. X., SONG, J. H., LIU, J., and WANG, Z. L. Nanowire piezoelectric nanogenerators on plastic substrates as flexible power sources for nanodevices. *Advanced Materials*, **19**, 67–72 (2007)

[3] CHOI, M. Y., CHOI, D., JIN, M. J., KIM, I., KIM, S. H., CHOI, J. Y., LEE, S. Y., KIM, J. M., and KIM, S. W. Mechanically powered transparent flexible charge-generating nanodevices with piezoelectric ZnO nanorods. *Advanced Materials*, **21**, 2185–2189 (2009)

[4] ROMANO, G., MANTINI, G., GARLO, A. D., D'AMICO, A., FALCONI, C., and WANG, Z. L. Piezoelectric potential in vertically aligned nanowires for high output nanogenerators. *Nanotechnology*, **22**, 465401 (2011)

[5] BÜYÜKKÖSE, S., HERNANDEZ-MINGUEZ, A., VRATZOV, B., SOMASCHINI, C., GEELHAAR, L., RIECHERT, H., WIE DER VAN, W. G., and SANTOS, P. V. High-frequency acoustic charge transport in GaAs nanowires. *Nanotechnology*, **25**, 135204 (2014)

[6] LIU, W., ZHANG, A. H., ZHANG, Y., and WANG, Z. L. First principle simulations of piezotronic transistors. *Nano Energy*, **14**, 355–363 (2015)

[7] WU, Y. R. and SINGH, J. Metal piezoelectric semiconductor field effect transistors for piezoelectric strain sensors. *Applied Physics Letters*, **85**, 1223–1225 (2004)

[8] WANG, Z. L. ZnO nanowire and nanobelt platform for nanotechnology. *Materials Science and Engineering*: *R*: *Reports*, **64**, 33–71 (2009)

[9] ZHAO, Z. F., PU, X., HAN, C. B., DU, C. H., LI, L. X., JIANG, C. Y., HU, W. G., and WANG, Z. L. Piezotronic effect in polarity-controlled GaN nanowires. *ACS Nano*, **9**, 8578–8583 (2015)

[10] WANG, Z. L. Novel nanostructures of semiconducting oxides. *Advanced Materials*, **15**, 432–436 (2003)

[11] ZHANG, C. L., WANG, X. Y., CHEN, W. Q., and YANG, J. S. An analysis of the extension of a ZnO piezoelectric semiconductor nanofiber under an axial force. *Smart Materials and Structures*, **26**, 025030 (2017)

[12] GAO, Y. F. and WANG, Z. L. Electrostatic potential in a bent piezoelectric nanowire. The fundamental theory of nanogenerator and nanopiezotrionics. *Nano Letters*, **7**, 2499–2505 (2007)

[13] GAO, Y. F. and WANG, Z. L. Equilibrium potential of free charge carriers in a bent piezoelectric semiconductive nanowire. *Nano Letters*, **9**, 1103–1110 (2009)

[14] FAN, S. Q., LIANG, Y. X., XIE, J. M., and HU, Y. T. Exact solutions to the electromechanical quantities inside a statically-bent circular ZnO nanowire by taking into account both the piezoelectric property and the semiconducting performance: part I — linearized analysis. *Nano Energy*, **40**, 82–87 (2017)

[15] LIANG, Y. X., FAN, S. Q., CHEN, X. D., and HU, Y. T. Nonlinear effect of carrier drift on the performance of an n-type ZnO nanowire nanogenerator by coupling piezoelectric effect and semiconduction. *Beilstein Journal of Nanotechnology*, **9**, 1917–1925 (2018)

[16] LEW, L. C., VOON, Y., and WILLATZEN, M. Electromechanical phenomena in semiconductor nanostructures. *Journal of Applied Physics*, **109**, 031101 (2011)

[17] ZHANG, R. Y. and HU, H. P. A few transient effects in AT-cut quartz thickness-shear resonators. *IEEE Transactions on Ultrasonics Ferroelectrics & Frequency Control*, **58**, 2758–2762 (2011)

[18] ZHANG, Y., LIU, Y., and WANG, Z. L. Fundamental theory of piezotronics. *Advanced Materials*, **23**, 3004–3013 (2011)

[19] LUO, Y. X., CHENG, R. R., ZHANG, C. L., CHEN, W. Q., and YANG, J. S. Electromechanical fields near a circular PN junction between two piezoelectric semiconductors. *Acta Mechanica Solida Sinica*, **31**, 127–140 (2018)

[20] YANG, W. L., FAN, S. Q., LIANG, Y. X., and HU, Y. T. Prestress-loading effect on the current-voltage characteristics of a piezoelectric p-n junction together with the corresponding mechanical tuning laws. *Beilstein Journal of Nanotechnology*, **10**, 1833–1843 (2019)

[21] YANG, G. Y., YANG, L., DU, J. K., WANG, J., and YANG, J. S. PN junctions with coupling to bending deformation in composite piezoelectric semiconductor fibers. *International Journal of Mechanical Sciences*, **173**, 105421 (2020)

[22] JIAO, F. Y., WEI, P. J., ZHOU, X. L., and ZHOU, Y. H. The dispersion and attenuation of the multi-physical fields coupled waves in a piezoelectric semiconductor. *Ultrasonics*, **92**, 68–78 (2019)

[23] JIAO, F. Y., WEI, P. J., ZHOU, Y. H., and ZHOU, X. L. Wave propagation through a piezoelectric semiconductor slab sandwiched by two piezoelectric half-spaces. *European Journal of Mechanics-A/Solids*, **75**, 70–81 (2019)

[24] ZHU, F., JI, S. H., QIAN, Z. H., and YANG, J. S. Study on the influence of semiconductive property for the improvement of nanogenerator by wave mode approach. *Nano Energy*, **52**, 474–484 (2018)

[25] CAO, X. S., HU, S. M., LIU, J. J., and SHI, J. P. Generalized Rayleigh surface waves in a piezoelectric semiconductor half space. *Meccanica*, **54**, 271–281 (2019)

[26] QU, Y. L., JIN, F., and YANG, J. S. Torsion of a flexoelectric semiconductor rod with a rectangular cross section. *Archive of Applied Mechanics*, **91**, 2027–2038 (2021)

[27] DAI, X. Y., ZHU, F., QIAN, Z. H., and YANG, J. S. Electric potential and carrier distribution in a piezoelectric semiconductor nanowire in time-harmonic bending vibration. *Nano Energy*, **43**, 22–28 (2018)

[28] ZHI, W., ZHAO, M. H., and YANG, J. S. Amplitude evolution equation and transient effects in piezoelectric crystal resonators. *Journal of Applied Physics*, **114**, 144510 (2013)

[29] LIANG, Y. X., YANG, W. L., and YANG, J. S. Transient bending vibration of a piezoelectric semiconductor nanofiber under a suddenly applied shear force. *Acta Mechanica Solida Sinica*, **32**, 688–697 (2019)

[30] YANG, W. L., HU, Y. T., and YANG, J. S. Transient extensional vibration in a ZnO piezoelectric semiconductor nanofiber under a suddenly applied end force. *Materials Research Express*, **6**, 025902 (2018)

[31] ZHANG, C. L., WANG, X. Y., CHEN, W. Q., and YANG, J. S. Propagation of extensional waves in a piezoelectric semiconductor rod. *AIP Advances*, **6**, 045301 (2016)

[32] AULD, B. A. *Acoustic Fields and Waves in Solids*, Vol. I, Wiley, New York (1973)

[33] LIANG, Y. X. and HU, Y. T. Effect of interaction among the three time scales on the propagation characteristics of coupled waves in a piezoelectric semiconductor rod. *Nano Energy*, **68**, 104345 (2020)

[34] ARFKEN, G. B. and WEBER, H. J. *Mathematical Methods for Physicists*, 4th ed., Academic Press, San Diego (1995)

Appendix A

The simplified theoretical analysis is carried out in this appendix. As an approximation often used in Refs. [12] and [29]–[31], the charge on the right-hand side of Eq. (1b) is neglected to decouple the problem into two one-way coupled problems, i.e., the pure piezoelectric problem and the continuity equation for Δn.

The pure piezoelectric problem consists of the following equations:

$$T_{3,3} = \rho \ddot{u}_3, \tag{A1a}$$

$$D_{3,3} = 0. \tag{A1b}$$

Using Eqs. (2a) and (2b), Eq. (A1) can be rewritten as

$$\begin{cases} \overline{c}_{33}u_{3,33} + \overline{e}_{33}\varphi_{,33} = \rho\ddot{u}_3, \\ \overline{e}_{33}u_{3,33} - \overline{\varepsilon}_{33}\varphi_{,33} = 0. \end{cases} \tag{A2}$$

From Eq. (4) and Eq. (A1b), we can obtain $D_3 = 0$ at the domain, which represents $\overline{e}_{33}u_{3,3} = \overline{\varepsilon}_{33}\varphi_{,3}$. Therefore, the axial stress can be simplified as

$$T_3 = \overline{c}_{33}u_{3,3} + \overline{e}_{33}\varphi_{,3} = c^*_{33}u_{3,3}, \tag{A3}$$

where

$$c^*_{33} = \overline{c}_{33}(1 + \overline{e}^2_{33}/(\overline{c}_{33}\overline{\varepsilon}_{33})), \tag{A4}$$

which is a piezoelectrically stiffened elastic constant. Then, Eqs. (A1a) and (4) can be rewritten as

$$\begin{cases} c^*_{33}u_{3,33} = \rho\ddot{u}_3, \\ u_3 = 0, \quad x_3 = 0, \\ c^*_{33}u_{3,3} = T, \quad x_3 = L, \\ u_3 = 0, \quad \dot{u}_3 = 0, \quad t = 0. \end{cases} \tag{A5}$$

To homogenize the boundary conditions in Eq. (A5), let

$$u_3 = u + Tx_3/c^*_{33}. \tag{A6}$$

Then, the problem for u is

$$c^*_{33}u_{,33} = \rho(\ddot{u} + \ddot{T}x_3/c^*_{33}), \tag{A7}$$

$$\begin{cases} u = 0, \quad x_3 = 0, \\ c^*_{33}u_{,3} = 0, \quad x_3 = L, \end{cases} \tag{A8}$$

$$u = 0, \quad \dot{u} + \dot{T}(0)x/c^*_{33} = 0, \quad t = 0. \tag{A9}$$

Mathematically, the solutions of u can be obtained by the method of separation of variables[34],

$$u(x_3, t) = v(x_3, t) + w(x_3, t), \tag{A10}$$

where

$$\begin{cases} v(x_3,t) = \displaystyle\sum_{m=0}^{\infty} V_m(t)\sin((\pi + 2m\pi)x_3/(2L)), \\ V_m(t) = \dfrac{2L}{(\pi + 2m\pi)c}\displaystyle\int_0^t g_m(\tau)\sin((\pi + 2m\pi)c(t-\tau)/(2L))\mathrm{d}\tau, \quad m = 0, 1, 2, \cdots, \\ g_m(t) = \dfrac{2}{L}\displaystyle\int_0^L (-\ddot{T}x_3/c^*_{33})\sin((\pi + 2m\pi)x_3/(2L))\mathrm{d}x_3, \quad c = \sqrt{c^*_{33}/\rho}, \end{cases} \tag{A11}$$

$$\begin{cases} w(x_3,t) = \displaystyle\sum_{n=0}^{\infty} (A_n\sin((\pi + 2m\pi)ct/(2L)))\sin((\pi + 2m\pi)x_3/(2L)), \\ A_m = \dfrac{4}{(\pi + 2m\pi)c}\displaystyle\int_0^L (-\dot{T}(0)x_3/c^*_{33})\sin((\pi + 2m\pi)x_3/(2L))\mathrm{d}x_3, \quad m = 0, 1, 2, 3, \cdots. \end{cases} \tag{A12}$$

Once u is obtained, u_3 and φ are obtained from Eqs. (A6) and (A2), respectively. Due to $\overline{e}_{33}u_{3,3} = \overline{\varepsilon}_{33}\varphi_{,3}$ and $N_{\mathrm{D}} = n_0$ because of uniform impurity, the equation for Δn is obtained from Eq. (1c) and Eq. (2c) as

$$\Delta\dot{n} = -n_0\mu^n_{33}\overline{e}_{33}u_{3,33}/\overline{\varepsilon}_{33} + D^n_{33}\Delta n_{,33} \tag{A13}$$

with the following boundary and initial conditions:

$$J_3 = -qn_0\mu_{33}^n\overline{e}_{33}u_{3,3}/\overline{\varepsilon}_{33} + qD_{33}^n\Delta n_{,3} = 0, \quad x_3 = 0, L, \tag{A14}$$

$$\Delta n = 0, \quad t = 0. \tag{A15}$$

To make the boundary conditions in Eq. (A14) homogeneous, the solution of Δn can be obtained by separation of variables and the Laplace transform[34]. Therefore, let

$$\Delta n = \widehat{n} + n_0\mu_{33}^n\varphi/D_{33}^n. \tag{A16}$$

The initial-boundary value problem for $\widehat{n}$ is

$$\dot{\widehat{n}} = D_{33}^n\widehat{n}_{,33} - n_0\mu_{33}^n\dot{\varphi}/D_{33}^n, \tag{A17}$$

$$\widehat{n}_{,3} = 0, \quad x_3 = 0, L, \tag{A18}$$

$$\widehat{n} = 0, \quad t = 0. \tag{A19}$$

Equations (A17)–(A19) are also a standard mathematical problem, whose solution by separation of variables and the Laplace transform is

$$\widehat{n}(x_3, t) = \sum_{r=0}^{\infty}\Big(\int_0^t a_r(\tau)\mathrm{e}^{-(r\pi\sqrt{D_{33}^n}/L)^2(t-\tau)}\mathrm{d}\tau\cdot\cos(r\pi x_3/L)\Big), \tag{A20}$$

where

$$\begin{cases} a_0(t) = \dfrac{1}{L}\displaystyle\int_0^L(-n_0\mu_{33}^n\dot{\varphi}/D_{33}^n)\mathrm{d}x_3, \quad r = 0, \\ a_r(t) = \dfrac{2}{L}\displaystyle\int_0^L(-n_0\mu_{33}^n\dot{\varphi}/D_{33}^n)\cos(r\pi x_3/L)\mathrm{d}x_3, \quad r = 1, 2, 3, \cdots. \end{cases} \tag{A21}$$